

# Noninvasive In Vivo Determination of Residual Strains and Stresses

**Samir Donmazov**

Department of Mechanical Engineering,  
Koç University,  
Sariyer, Istanbul 34450, Turkey

**Senol Piskin**

Department of Mechanical Engineering,  
Koç University,  
Sariyer, Istanbul 34450, Turkey

**Kerem Pekkan<sup>1</sup>**

Associate Professor  
Department of Mechanical Engineering,  
Koç University,  
Rumelifeneri Kampüsü,  
Sariyer, Istanbul 34450, Turkey;  
Department of Biomedical Engineering,  
Carnegie Mellon University,  
Pittsburgh, PA 15219  
e-mail: kpekk@ku.edu.tr

*Vascular growth and remodeling during embryonic development are associated with blood flow and pressure induced stress distribution, in which residual strains and stresses play a central role. Residual strains are typically measured by performing in vitro tests on the excised vascular tissue. In this paper, we investigated the possibility of estimating residual strains and stresses using physiological pressure–radius data obtained through in vivo noninvasive measurement techniques, such as optical coherence tomography or ultrasound modalities. This analytical approach first tested with in vitro results using experimental data sets for three different arteries such as rabbit carotid artery, rabbit thoracic artery, and human carotid artery based on Fung's pseudostrain energy function and Delfino's exponential strain energy function (SEF). We also examined residual strains and stresses in the human swine iliac artery using the in vivo experimental ultrasound data sets corresponding to the systolic-to-diastolic region only. This allowed computation of the in vivo residual stress information for loading and unloading states separately. Residual strain parameters as well as the material parameters were successfully computed with high accuracy, where the relative errors are introduced in the range of 0–7.5%. Corresponding residual stress distributions demonstrated global errors all in acceptable ranges. A slight discrepancy was observed in the computed reduced axial force. Results of computations performed based on in vivo experimental data obtained from loading and unloading states of the artery exhibited alterations in material properties and residual strain parameters as well. Emerging noninvasive measurement techniques combined with the present analytical approach can be used to estimate residual strains and stresses in vascular tissues as a precursor for growth estimates. This approach is also validated with a finite element model of a general two-layered artery, where the material remodeling states and residual strain generation are investigated. [DOI: 10.1115/1.4030071]*

## 1 Introduction

Residual stresses play a central role in cardiovascular soft tissue mechanics as they influence the observed in vivo material response significantly and hypothesized to be an essential factor for the healthy physiology of the vascular lumen and matrix maintenance [1]. Residual stresses exist in both arteries and veins, even when all external loadings are removed. They are generated due to deformations known as residual strains within the tissue wall associated with kinematic compatibility constraints as well as vascular growth and remodeling such as new matrix synthesis or smooth muscle activation.

Numerous studies emphasized the structural function of the residual strains [2,3]. Particularly, residual strains pose a well-known ability to homogenize the stress distribution in the arterial wall thus optimizes the load bearing capability. In addition, they can also make arteries more compliant by providing a nonlinear elastic nature to address with high pressure levels and exhibit more effective local control over the arterial diameter by means of smooth muscle cell activation [4]. Therefore, residual stresses are essential for the physiological vascular control or can act as a structural optimization agent that can be preferred over vascular remodeling, which requires more expensive matrix synthesis.

While there exist a variety of noninvasive techniques to measure residual stresses that are amiable to industrial applications [5,6], for biomedical applications residual stresses are measured

through in vitro experiments of excised vessel specimens, where geometric constraints are removed sequentially through invasive directional vessel cuts. This well-established experimental technique is pioneered by Chuong and Fung, who conducted in vitro experiments [7] and determined the residual strains in a rabbit thoracic artery at its *unloaded state* by measuring the effective angle, inner radius, and outer radius in zero-stress configuration and inner radius in unloaded state [8]. Another approach, proposed by Takamizawa and Hayashi, was that circumferential strain is assumed to be constant through the dog carotid artery arterial wall cross section under physiological loading condition, so that the computed circumferential stress distribution was almost uniform [9]. Through this assumption, the existence of residual strains and stresses within the wall became evident. Several subsequent investigations confirmed the existence of residual strains in different arteries, besides in other cylindrically shaped soft tissues such as the left ventricle [10–12], veins [13,14], trachea [15], brain [16], and embryonic ventricle [17]. Thus far, no one considered the significance of the axial prestretch. Later, Alford and Taber [18] showed that arteries with delayed elastin production grow longer than arteries in which elastin is produced early in development and in the presence of axial growth, the stretch has no effect on the opening angle (i.e., effective angle). In contrast, if axial growth does not occur, then the opening angle depends strongly on the in vivo axial prestretch. Soon after, Wang and Gleason described the use of longitudinal opening angle, since based on their conclusion the radial cut of the arterial ring segment cannot describe the zero-stress reference configuration of arteries [19].

<sup>1</sup>Corresponding author.

Manuscript received November 6, 2014; final manuscript received March 6, 2015; published online April 15, 2015. Assoc. Editor: Thao (Vicky) Nguyen.

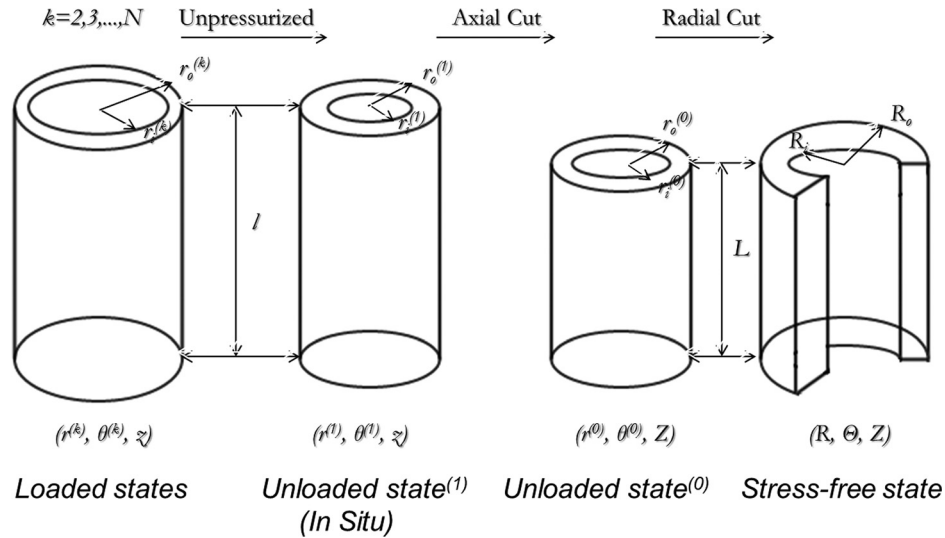


**Fig. 1 General geometrical representation of 3D vessel wall in zero-stress reference state, unloaded state<sup>(0)</sup>, unloaded state<sup>(1)</sup>, and subsequent loaded states under transmural pressure and axial forces**

The material properties of vascular soft tissues are remodeled in vivo due to physiological, genetic, mechanical, and environmental factors [20]. For example, embryonic tissue becomes less compliant with age due to collagen synthesis. Likewise, smoking and high blood pressure make blood vessels to become stiffer but at a different timescale. While it is not straightforward to differentiate residual stresses from material properties, it is hypothesized that residual stresses should also change dramatically during vascular remodeling and embryonic vascular growth, similar to the material properties. To extract this important parameter, a noninvasive experimental methodology is developed to track and quantify the in vivo residual stress levels in the vascular tissue. Therefore in this paper, we present an analytical approach to estimate the vascular residual stresses in vivo at cylindrical vessels through noninvasive measurements of pressure and vessel geometry.

The present paper is organized as follows: In Sec. 2 constitutive relations, numerical approximation, finite element model, and various test cases are presented, followed by the key aspects of the present computational algorithm. In Sec. 3, first the effects of increase in experimental data points, addition of Gaussian noise to the data set obtained from the diastolic–systolic pressure range and choice of different SEF are examined for in vitro validation of material parameters and residual strain parameters and the residual stress distribution computed for each artery is compared with corresponding result based on in vitro tests. In the second part, material parameters, residual strain parameters, and corresponding residual stress distribution are computed for swine iliac artery based on in vivo experimental data. In Sec. 4, we analyze the predictive capability and limitations of present mathematical approach by discussing computed results and its possible future application on the embryonic chick vessel. In Sec. 5, we also discuss the advantages of present *noninvasive* technique on the prediction of pediatric vessel growth over *invasive* classical experimental methods.

## 2 Methods

A general formulation is proposed to determine the effective angle and the effective radii in stress-free state, unloaded inner radius, and in vivo axial prestretch in order to estimate residual strains and stresses from standard *noninvasive* measurement techniques. This approach also allowed the prediction of vascular material properties with reasonable accuracy. For brevity, the

methodology is illustrated here using the stain energy formulation but it can be easily formulated for more complex multistructural material models [21–23].

**2.1 Representation of the Vascular Loading States.** In Fig. 1, 3D axisymmetric vessel wall is presented at its key loading states. The vascular lumen is treated as a cylindrical tube assuming that it has homogeneous material properties through the wall and it is cylindrically orthotropic. Another assumption is that the vessel wall should become an open sector with constant curvature after removing residual stresses from unloaded state<sup>(0)</sup>. We also assumed that the vessel length does not change during the transformation from stress-free state to unloaded state<sup>(0)</sup>. Additionally, the axial prestretch is taken into account while transforming the unloaded state<sup>(0)</sup> into unloaded state<sup>(1)</sup>. Subsequent loaded states are defined as state 2, 3, ..., *N*. Coordinates of material points in described states are  $(R, \Theta, Z)$ ,  $(r^{(1)}, \theta^{(1)}, z)$ ,  $(r^{(k)}, \theta^{(k)}, z)$  for  $k = 2, 3, \dots, N$ , respectively. Similarly, backward subsequent unloading states for  $k = N, N-1, \dots, 2$  are required to represent viscoelastic nature of soft tissues as the variation in mechanical and material properties due to the previous corresponding effects of loading states. Subscripts *i* and *o* denote the inner and outer wall radii at various states, and  $\Theta_0$  represents half of the angle of open sector at stress-free configuration.

In addition to the Fung's representation of states of artery [8] in the present formulation, an intermediate unloaded state<sup>(1)</sup> is included. This new intermediate loading state corresponds to the case with zero intramural pressure, but with the in vivo axial prestretch. After cutting the vessel axially, it is shortened and its radii are changed. Finally, making radial cut releases all residual stresses and cylindrical tube becomes an open sector with the same length but with altered radii.

**2.2 Constitutive Relations.** The finite theory of plane strain deformation leads the following description for the residual circumferential and radial stretch ratios for homogeneous and cylindrically orthotropic arterial wall [8]:

$$\lambda_\theta = \frac{\pi r}{\Theta_0 R}, \quad \lambda_r = \frac{1}{\lambda_\theta \lambda_z}, \quad \Theta_0 = \pi - \alpha \quad (1)$$

$$r = \sqrt{r_i^2 + \frac{\Theta_0}{\pi} (R^2 - R_i^2)}, \quad R_i \leq R \leq R_o$$

where  $\theta$  and  $\alpha$  are the effective angle and the opening angle, respectively.  $r$  and  $R$  are the radii of an arbitrary point, and  $r_i$  and  $R_i$  the inner radii in the unloaded and stress-free state, respectively.  $R_o$  is the outer radius in the stress-free configuration.

It is assumed that the deformation in the longitudinal direction occurs only during the transformation from unloaded state<sup>(0)</sup> into unloaded state<sup>(1)</sup>, rather than from zero-stress state into unloaded state<sup>(0)</sup> does not occur, the corresponding residual Green strains are

$$E_\theta = \frac{1}{2}(\lambda_\theta^2 - 1), \quad E_r = \frac{1}{2}(\lambda_r^2 - 1), \quad E_z = \frac{1}{2}(\lambda_z^2 - 1) \quad (2)$$

In the present paper, we selected and tested two classical SEFs, Fung's exponential pseudostrain energy function [24] and Delfino's exponential SEF [25], to verify and illustrate our mathematical approach.

Fung's exponential pseudostrain energy function is given by

$$\rho_0 W = \frac{c}{2} e^Q \quad (3)$$

where

$$Q = b_1 E_\theta^2 + b_2 E_z^2 + b_3 E_r^2 + 2b_4 E_\theta E_z + 2b_5 E_z E_r + 2b_6 E_r E_\theta \quad (4)$$

Since the arterial wall is assumed to be an incompressible, SEF is modified by adding a Lagrangian multiplier to handle the incompressibility condition explicitly. This condition can be released if needed but kept here for simplicity. After defining the transformation from the reference state to the deformed state in terms of the coordinates  $X_\alpha$  and  $x_i$  in the undeformed and deformed states, respectively, Cauchy stress components are obtained as

$$\sigma_{ij} = \frac{\rho}{\rho_0} \frac{\partial x_j}{\partial X_\alpha} \frac{\partial x_i}{\partial X_\beta} \frac{\partial}{\partial E_{\beta\alpha}} \rho_0 W^*, \quad (i, j, \alpha, \beta = r, \theta, z) \quad (5)$$

where  $\rho$  and  $\rho_0$  correspond to the densities of material in the deformed and undeformed states, respectively, and  $\rho_0 W^*$  is the modified SEF.

For the Delfino's exponential SEF,

$$\bar{\Psi} = \frac{a}{b} \left\{ \exp \left[ \frac{b}{2} (\bar{I}_1 - 3) - 1 \right] \right\} \quad (6)$$

Cauchy stress tensor due to isochoric effect is given by

$$\bar{\sigma} = 2\bar{\Psi}_1 \text{dev} \bar{b} \quad (7)$$

where  $\bar{\Psi}_1 = \partial \bar{\Psi} / \partial \bar{I}_1$  and  $\bar{b}$  are the modified left Cauchy–Green tensor and the operator, and the operator  $\text{dev}(\bullet)$  is defined by

$$\text{dev}(\bullet) = (\bullet) - \frac{1}{3} [(\bullet) : I] I \quad (8)$$

Note that for nearly incompressible material  $J \approx 1$ .

Finally, the pressure integral equation is obtained substituting the circumferential and radial Cauchy stress components into the radial equilibrium equation, and integrating in terms of radii from the undeformed configuration

$$p_i = \int_{R_i}^{R_o} c[(1 + 2E_\theta)(b_1 E_\theta + b_4 E_z + b_6 E_r) - (1 + 2E_r) \times (b_6 E_\theta + b_5 E_z + b_3 E_r)] e^Q \frac{R}{R^2 - R_i^2 + \frac{180\lambda_z r_i^2}{\Theta_0}} dR \quad (9)$$

Since the measurement of axial force requires *invasive* techniques, the axial force equilibrium is not taken into account explicitly.

**2.3 Numerical Integration Framework.** Gauss quadrature formula for a general case is given by

$$\int_a^b f(x) dx \approx \frac{b-a}{2} \sum_{i=1}^n w_i f\left(\frac{b-a}{2} x_i + \frac{a+b}{2}\right) \quad (10)$$

where  $a$  and  $b$  are the lower and upper bounds of the integral, respectively,  $n$  is the number of (nodes) the roots, and  $x_i$  is the  $i$ th root of the  $n$ th order Legendre polynomials; its weight  $w_i$  is given by

$$w_i = \frac{2}{(1 - x_i^2) [P'_n(x_i)]^2} \quad (11)$$

For present problem, radium equilibrium equation is written in its compact form, in terms of circumferential and radial stress components

$$p_i = \int_{R_i}^{R_o} (\sigma_\theta - \sigma_r) \frac{R}{R^2 - R_i^2 + 180\lambda_z r_i^2 / \Theta_0} dR \quad (12)$$

Gaussian quadrature formula is given by

$$p_i \approx \sum_{j=0}^5 w_j f(R_j) \frac{R_j}{R_j^2 - R_i^2 + 180\lambda_z r_i^2 / \Theta_0} \quad (13)$$

Pressure integral function is discretized by using Gaussian Quadrature formula, where  $R_j$  are quadrature nodes and roots of sixth order Legendre polynomial  $L_6(R) \in P_6$  in the interval  $[R_i, R_o]$  with degree of exactness “11,” which gives the exact solution for  $P_{11}$ .

Two separate models model are presented based on discretized pressure function Eq. (13) for each strain energy formulation. For Fung's SEF, 10 parameters model (10 PM) is formulated in terms of seven material parameters and three residual strain parameters, where in vivo axial prestretch is assumed to be known and 11 parameters model (11 PM) additionally includes the axial prestretch as an unknown. For Delfino's SEF, 5 parameters model (5 PM) in terms of two material parameters and three residual strain parameters and 6 parameters model (6 PM) including the axial prestretch are introduced.

**2.4 Test Cases.** This technique is first tested against in vitro experiments where residual stress is also measured invasively. Invasive residual stress measurements are compared with present analytical predictions. Pressure–inner radius curves obtained by Rachev and Holzapfel for rabbit thoracic artery [4], rabbit carotid artery, and human carotid artery [22] are digitized to simulate experimental data sets with various sampling sizes. For instance, we sampled 10, (9 + 1), 11 (9 + 2), 17, and 33 data points from the pressure interval of 0–160 mm Hg corresponding to the pressure increments of 20, 10, and 5 mm Hg, respectively. 10 and 11 data points were considered as a minimum experimental data set conditions for 10 PM and 11 PM, respectively. In general, the noninvasive in vivo physiological measurements will be limited to the cardiac cycle loading conditions. To illustrate this effect, 16 experimental data points covering the diastolic–systolic pressure range (approximately 60–120 mm Hg) are also utilized for the proposed residual stress prediction technique. In this study, we applied our technique to three artery types, having significantly different material properties represented by two different strain energy formulations. In addition, we studied the effect of

**Table 1** Experimental data sets with known residual stress and material properties where the present analytical approach is tested. The effect of more resolved experimental data sets is simulated by increased experimental data points obtained through higher-order digitizing procedure. Likewise, synthetic experimental error is included to verify the robustness of present approach. A large range of arterial material properties for rabbit carotid and thoracic artery as well as human carotid artery is tested subject to two different strain energy formulations. The effect of adding experimental noise to the same experimental data set from diastolic–systolic pressure region is also analyzed for each artery type.

Invasive measurements	Pressure range (mm Hg)	Number of data points tested
Rabbit carotid artery Fung's SEF [21]	0–160	10, 11, 17, 33, 16
Rabbit thoracic artery Fung's SEF [4]	0–180	10, 11, 19, 37, 16
Human carotid artery Delfino's SEF [21]	0–200	11, 21, 41, 16

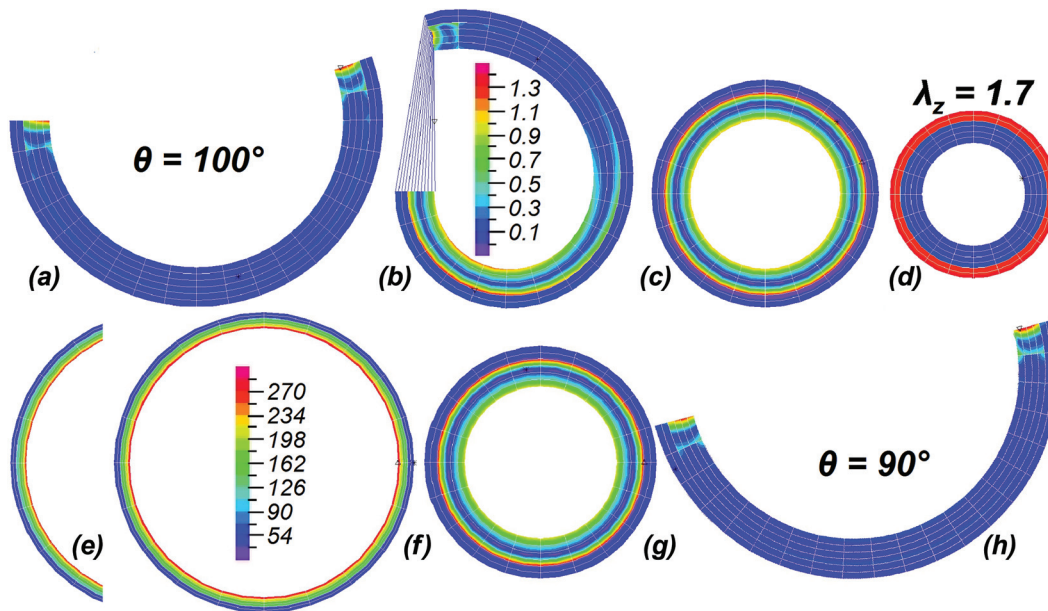


**Fig. 2** The two-layer microstructure finite element model of residual stress generation. Series of vessel cross sections representing: (a) the stress-free open configuration of the baseline rabbit carotid artery having an effective angle of 100 deg, (b) midvessel closure toward the fully closed unloaded state achieved by thrust elements pulling the open ends, (c) unloaded state<sup>(0)</sup>, (d) unloaded state<sup>(1)</sup> with prestretch—only mesh shown, and (e) the loaded state<sup>(2)</sup>—section of vessel is shown. Material properties are then altered representing the vascular remodeling by (f) the remodeled loaded state<sup>(3)</sup> and its corresponding (g) remodeled unloaded configuration and (h) remodeled stress-free state resulting in an effective angle of 90 deg. Color and legends correspond to the magnitude of Cauchy stress distributions (mm Hg). Legend in (f) corresponds to vessel cross sections in (e) and (f), while legend in (b) corresponds to all other states.

experimental noise on residual stress estimates. Complete experimental validation matrix is provided in Table 1.

Beyond the in vitro validation, we used in vivo pressure–outer diameter experimental data set for swine iliac artery [26] to estimate residual strains and stresses based on Fung's SEF. To give an insight about in vivo measurement technique of obtaining relevant data sets, in vivo measurements were performed on eight swine iliac arteries and the mean of pressure–outer diameter data points was obtained, where the outer diameter of arteries was measured by using the periarterial dimensional clip-probe imaging technique during the physiological loading and unloading states, and intravascular measurements of pulsatile blood pressure were performed with a pressure transducer.

**2.5 Notes on the Computational Algorithm.** A standard nonlinear least-squares curve fitting is implemented for each experimental data set with the objective function of discretized pressure function, using the *trust-region-reflective algorithm* for constrained optimization problem. In order to guarantee the convergence to physical local minima, it is essential to choose an appropriate physical interval for each variable. For example, by its definition material parameters appearing in both SEFs must be

positive real numbers, the effective angle  $\Theta_0$  is defined in the interval 0–180 deg, the axial prestretch  $\lambda_z$  is searched in the interval 1.0–2.0, and the effective radii are expected to be greater than the radii corresponding to the minimal in vivo pressure value of 60 mm Hg for each in vitro case, 123 mm Hg for swine iliac artery, and less than twice of these values.

## 2.6 Finite Element Model of Residual Stress Generation.

The three-dimensional finite element model of a circular artery is developed using ADINA (ADINA R&D, Inc., Watertown, MA) for further validation of the proposed formulation. The loading states in Fig. 1 including material remodeling are simulated sequentially using wires to achieve vessel closure from stress-free states. Snapshots from this model are plotted in Fig. 2 with boundary wire elements closing open ends to achieve residual stress generation in Fig. 2(b). The artery geometry is specified as a thick-walled cylindrical tube subjected to external loading with 120 hexahedral elements as shown in Fig. 2(d). Existence of compatibility conditions between each of the loading state is verified. The arterial wall is modeled as a two-layer (media and adventitia) incompressible hyperelastic fiber orientation model [22]. Each layer of the artery is modeled as a cylindrical orthotropic fiber-



**Table 2 Numerical values of 10 PM, where material parameters and residual strain parameters are computed using 10, 17, and 33 experimental data points for rabbit carotid artery compared with results based on in vitro experiments. [22] Boldface values appearing in table are directly cited from Ref. [22].**

Number of data points	$c$ (kPa)	Material parameters						Residual strain parameters		
		$b_1$	$b_2$	$b_3$	$b_4$	$b_5$	$b_6$	$\Theta_0$ (deg)	$R_i$ (mm)	$R_o$ (mm)
10	27.71	0.9942	0.4126	0.0089	0.0747	0.0227	0.0271	100.0	1.44	1.83
17	26.69	0.9922	0.4509	0.0004	0.0752	0.0181	0.0406	100.0	1.44	1.83
33	27.93	0.9935	0.4297	0.0029	0.0747	0.0280	0.0093	100.0	1.44	1.82
Ref.	<b>26.95</b>	<b>0.9925</b>	<b>0.4180</b>	<b>0.0089</b>	<b>0.0749</b>	<b>0.0295</b>	<b>0.0193</b>	<b>100.0</b>	<b>1.43</b>	<b>1.82</b>

**Table 3 Numerical values of constants appearing in 11 PM, where material parameters and residual strain parameters are computed using 10, 17, and 33 experimental data points for rabbit carotid artery compared with results based on in vitro experiments [22]. Boldface values appearing in table are directly cited from Ref. [22].**

Number of data points	$c$ (kPa)	Material parameters						Residual strain parameters			
		$b_1$	$b_2$	$b_3$	$b_4$	$b_5$	$b_6$	$\Theta_0$ (deg)	$R_i$ (mm)	$R_o$ (mm)	$\lambda_z$
11	27.24	0.9972	0.4418	0.0088	0.0747	0.0202	0.0253	99.9	1.45	1.83	1.71
17	27.29	0.9925	0.4204	0.0000	0.0750	0.0178	0.0409	100.1	1.44	1.83	1.71
33	27.59	0.9938	0.4482	0.0043	0.0747	0.0283	0.0075	100.0	1.44	1.81	1.71
Ref.	<b>26.95</b>	<b>0.9925</b>	<b>0.4180</b>	<b>0.0089</b>	<b>0.0749</b>	<b>0.0295</b>	<b>0.0193</b>	<b>100.0</b>	<b>1.43</b>	<b>1.82</b>	<b>1.70</b>

**Table 4 Numerical values of constants appearing in 11 PM, where material parameters and residual strain parameters are computed using 16 experimental data points from the diastolic–systolic pressure range without (DS) and with the addition of Gaussian noise for rabbit thoracic artery in the order of 1 Pa and 0.01 mm (DSN1) and in the order of 1 mm Hg and 0.1 mm (DSN2) [8]. Boldface values appearing in table are directly cited from Ref. [8].**

Number of data points	$c$ (kPa)	Material parameters						Residual strain parameters			
		$b_1$	$b_2$	$b_3$	$b_4$	$b_5$	$b_6$	$\Theta_0$ (deg)	$R_i$ (mm)	$R_o$ (mm)	$\lambda_z$
DS	21.85	1.0921	0.4750	0.0352	0.0921	0.2270	0.0000	71.4	3.93	4.67	1.691
DSN1	24.30	1.0613	0.3791	0.0593	0.0890	0.0000	0.0496	71.4	3.92	4.53	1.691
DSN2	23.41	1.0697	0.4099	0.1207	0.0778	0.0002	0.0346	71.4	3.92	4.54	1.691
Ref.	<b>22.40</b>	<b>1.0672</b>	<b>0.4775</b>	<b>0.0499</b>	<b>0.0903</b>	<b>0.0585</b>	<b>0.0042</b>	<b>71.4</b>	<b>3.92</b>	<b>4.52</b>	<b>1.691</b>

reinforced composite. Layers are modeled with separate SEF and the neo-Hookean model is used to determine the isotropic response of each layer. Material parameters and dimensions of geometry are obtained from rabbit carotid artery [7,24].

### 3 Results

#### 3.1 In Vivo Validation

**3.1.1 Effect of Number of Experimental Data Points.** The accuracy of estimated residual strain parameters and material parameters for each artery is tested by altering the number of experimental data points corresponding to the pressure increment of 20 mm Hg, 10 mm Hg, and 5 mm Hg. The response of alteration in number of unknown parameters is also analyzed by introducing 10 PM and 11 PM. Table 2 shows results for 10 PM with increasing number of experimental data points, 10 (9 + 1), 17, and 33 data points, for rabbit carotid artery, where the pressure interval is given as 0–160 mm Hg. Although material parameters exhibit some level of deviations from results obtained based on in vitro experiments, due to their high sensitiveness regarding to the nonlinearity presented in Fung's SEF, the range of local error introduced in each material parameter is acceptable. Whereas the computed residual strain parameters corresponding to each experimental data set demonstrate better agreement. More particularly, the similar trend, relative error 0–3.4%, is preserved after addition of another unknown, the axial prestretch into the system (Table 3). In all cases, increase in number of experimental data points does not really affect the accuracy of results, but still causes slight improvement in values.

**3.1.2 Effect of Experimental Noise.** The effect of experimental noise is analyzed by adding Gaussian noise to experimental data points obtained from diastolic–systolic pressure range for each artery in the order of 1 Pa for internal pressure and 0.01 mm for inner radius. These error ranges correspond to a typical servo-null micropressure measurement. We also tested the effect of increased error ranges in the order of 1 mm Hg (133.22 Pa) and 0.1 mm for internal pressure and inner radius, respectively, which correspond to a large artery cuff pressure measurement scenario. Table 4 demonstrates a good quantitative agreement in predicting in vivo residual strain parameters together with material parameters for rabbit thoracic artery based on the same strain energy formulation.

**3.1.3 Parameters of Delfino's SEF.** Computed material parameters  $a$  and  $b$ , and residual strain parameters the effective angle  $\Theta_0$ , the effective radii  $R_i$  and  $R_o$ , and in vivo axial pre-stretch  $\lambda_z$  are presented in Table 5. Results show that choice of appropriate strain energy formulation has an impact on the estimation of parameters. Delfino's formulation leads to greater local errors (0.6–7.5%) in each parameter.

**3.1.4 Computation of Inner Radius in Unloaded States.** In order to determine residual strains defined as a transformation from stress-free state into unloaded state<sup>(0)</sup>, unloaded state<sup>(1)</sup>, and so on, additional parameters inner radii in both unloaded states are computed for each artery by using extrapolation after determining all parameters. Table 6 shows that results are consistent with experimental ones.

**Table 5 Numerical values of constants appearing in 6 PM, where material parameters and residual strain parameters are computed using 11, 21, 41 experimental data points and 16 experimental data points from the diastolic–systolic pressure range without (DS) and with the addition of Gaussian noise for human carotid artery based on Delfino’s SEF (DSN) [22]. Bold-face values appearing in table are directly cited from Ref. [22].**

Number of data points	Material parameters		Residual strain parameters			
	$a$ (kPa)	$b$	$\Theta_0$ (deg)	$R_i$ (mm)	$R_o$ (mm)	$\lambda_z$
11	38.72	18.13	127.1	4.58	5.76	1.08
21	47.15	16.44	130.0	4.43	5.33	1.08
41	39.85	17.58	135.4	4.27	5.40	1.08
DS	40.88	17.04	128.3	4.56	5.46	1.12
DSN	38.67	17.27	126.8	4.65	5.58	1.13
Ref.	<b>44.20</b>	<b>16.70</b>	<b>130.0</b>	<b>4.46</b>	<b>5.36</b>	<b>1.10</b>

**Table 6 Numerical values of inner radii in unloaded state<sup>(0)</sup> and unloaded state<sup>(1)</sup> compared with results based on in vitro experimental results for rabbit carotid artery [22], rabbit thoracic artery [8], and human carotid artery [22].**

Inner radius, $r_i$ (mm)	Unloaded state <sup>(0)</sup> (in situ)		Unloaded state <sup>(1)</sup>	
	Experimental	Computed	Experimental	Computed
Rabbit carotid artery	0.74	0.73	0.71	0.71
Rabbit thoracic artery	1.38	1.35	1.35	1.37
Human carotid artery	2.96	2.96	3.10	3.15

**3.1.5 Residual Stress Distribution.** Residual stress distributions in both unloaded states are plotted for all three arteries (Figs. 3–5). It can be deduced that the presence of axial prestretch in unloaded state<sup>(1)</sup> alters the residual stress distribution significantly and resulting in greater global error. Especially, for human carotid artery, estimated residual stresses significantly differ from its pairs obtained based on in vitro testing.

**3.1.6 Axial Force Equilibrium.** Axial force distribution through the arterial wall is plotted to check the validity of disregarding the axial force balance, since the measurement of axial force requires in vitro interventions. In Fig. 4, reduced axial force is computed for rabbit carotid artery and human carotid artery using Fung’s SEF and Delfino’s SEF. Although both plots are consistent with results obtained based on in vitro measurements, resulting global error for human carotid is greater because of high sensitive structure of Delfino’s SEF.

## 3.2 In Vivo Results

**3.2.1 Nonlinear Regression and Parameter Estimation.** Nonlinear least-squares curve fitting analysis is performed on experimental data sets, which were obtained from physiological state of swine iliac artery by using in vivo measurement techniques. Table 7 shows computed results for material parameters and residual strain parameters of swine iliac artery in loading and unloading states. Except in vivo axial prestretch, all other parameters demonstrate slight variations as expected. Increase in the material parameter  $c$  (kPa) indicates the stiffening of the arterial wall after subsequent loading steps.

**3.2.2 Residual Stress Distribution in Loading and Unloading States.** Inner radii of swine iliac artery in unloaded state<sup>(0)</sup> and unloaded state<sup>(1)</sup> are extrapolated at zero pressure using the pressure–outer radius relation curves, where the inner radii in unloaded state<sup>(0)</sup> and unloaded state<sup>(1)</sup> were computed as 2.63 mm and 1.91 mm for loading states, and 3.06 mm and 2.20 mm for unloading states, respectively.

Residual stresses are estimated in each unloaded state by using computed material parameters, residual strain parameters, and inner radius of relevant state. Since soft tissues demonstrate a viscoelastic mechanical response, residual stress distribution in loading states and unloading states treated separately. Figure 5 illustrates residual stresses for loading states and unloading states in the same plot without and with taking the existence of in vivo axial prestretch within the swine iliac artery into account.

**3.3 Remodeled States and Validation With Finite Element Model.** The finite element model allowed the generation of several synthetic experimental data sets for validation purposes. To illustrate the utilization of the present technique in a realistic growth and remodeling scenario, we simulated a remodeled artery from its baseline material properties. Our baseline model corresponds to the Fung’s artery model [7,24] having an effective opening angle of 100 deg. This artery is closed from its stress-free state where residual stress is generated and extended in the axial direction. Next, the artery is inflated with the specified intramural pressure levels. The resulting pressure–inner radius data are extracted from the finite element model and used in our optimization formulation as an input. Accurate agreement with the specified opening angle in the finite element model versus the present analytical approach is observed.

At this loaded baseline state, the material properties are altered which corresponds to a remodeled artery in silico. Baseline material properties are provided in Table 8. Then, the artery is deflated to zero pressure state and shortened to closure state. It is then cut again to obtain the effective angle at zero-stress state. The effective angle after remodeling is computed to be 90 deg. The pressure–radius data for the remodeled case are also used in our formulation and the remodeled effective angle is also computed accurately. In addition, the inner and outer radii were estimated for both cases, which were found within 10% vicinity. The results of these simulations are tabulated in Table 8. Stress distribution and geometry at several loading states including baseline and remodeled cases are presented in Fig. 2.

## 4 Discussion

Arterial and venous vessel growth is known to be associated with the level of residual stresses. The rate of growth is hypothesized to depend on the difference between the present stress level occurring due to the external loading and the homeostatic stresses, according to the Belousov’s hyper-restoration (HR) hypothesis [27]. HR hypothesis have not been fully validated through in vivo measurements due to the invasive nature of residual stress measurement techniques. Besides these experimental challenges, several studies indicate that residual stresses emerge as a result of elastic deformations occurring to ensure the compatibility of the growing tissue [28]. Thus, as a part of the total stress distribution, residual stresses play a significant role in the physiological and pathological growth process of the vascular system, while they arise due to the growth itself. This makes residual stresses and the growth and remodeling mutually interdependent. That is to say, knowledge of residual stresses can allow the prediction of vessel growth. This is particularly important for pediatric and fetal cardiac diseases and in their surgical repairs, since vascular growth should be incorporated in the therapy or surgical intervention design [29,30].

During the growth of vascular system, the alteration in material properties (remodeling) is present while the tissue tries to make ongoing deformations compatible, so that residual strains and stresses are generated. Nevertheless, the fundamental mechanism driving the vascular growth and remodeling is not completely understood [31]. It is also widely accepted that the level of local residual stresses induces growth according to the HR hypothesis as a result of deviation in local stresses due to external loadings from the homeostatic stress state and *noninvasive* techniques are required to track the residual stresses in time. Therefore, this

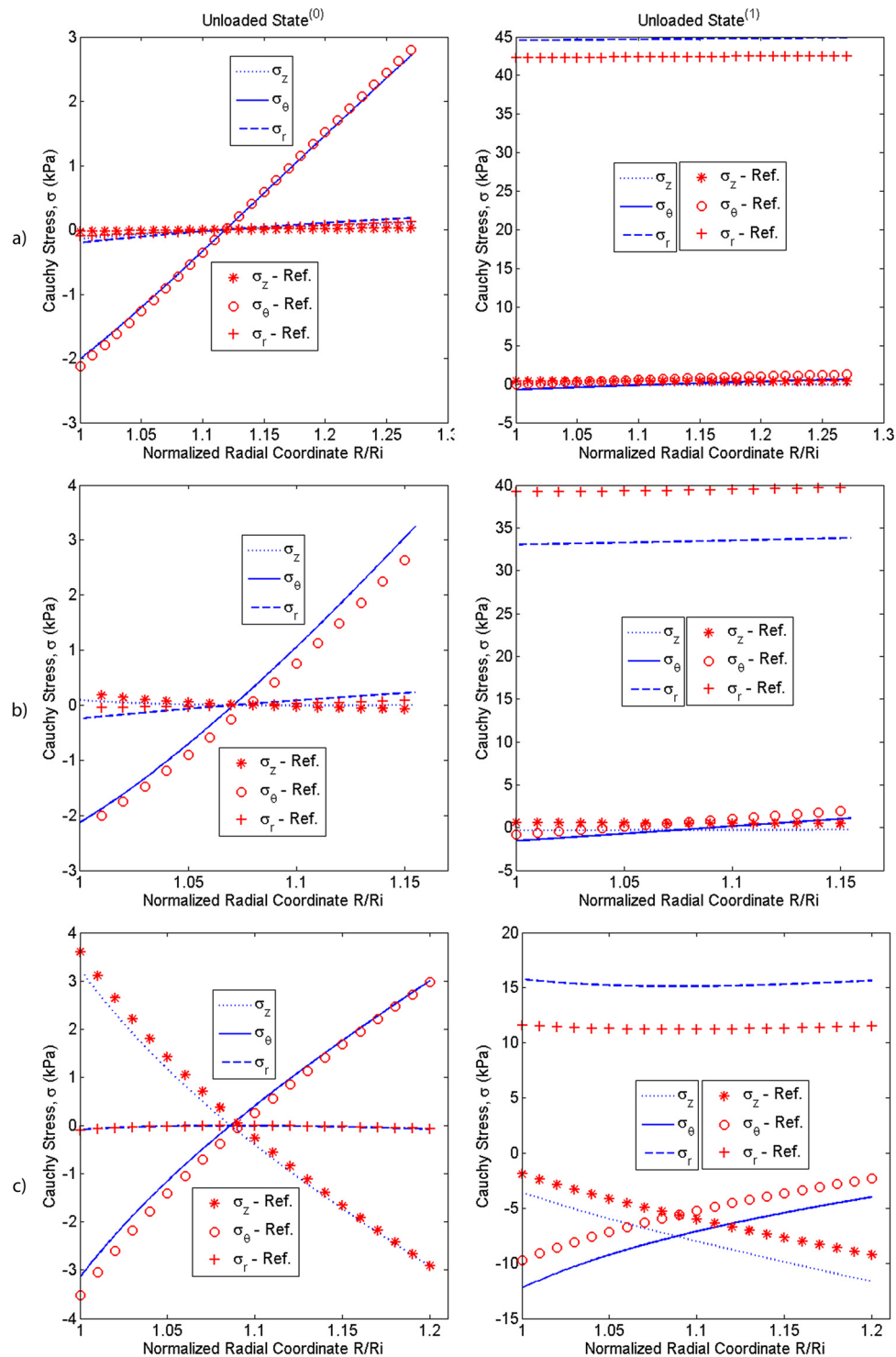


**Fig. 3 Residual stress distribution through the arterial wall in unloaded state<sup>(0)</sup> and unloaded state<sup>(1)</sup> in (a) rabbit carotid artery, (b) rabbit thoracic, and (c) human carotid artery, respectively, compared with experimental results based on in vitro data given in (a) Ref. [22], (b) Ref. [4], and (c) Ref. [22]**

paper focused on two aspects: first is the validation of the mathematical approach of computing residual strain parameters together with material parameters and corresponding residual strain and stresses with in vitro testing results, and the other is to estimate residual strains and stresses using experimental data sets obtained from in vivo measurement techniques.

The different features of the developed theoretical model influence its special numerical treatment. Naturally, ignoring the

physical constraint in the axial direction may cause the loss of information about the nonlinear system, where it is compensated by proper selection of constraints for each of the unknown parameters that guarantees the convergence to the physical local minima, though there are several local minima arising from the nonconvexity of present SEF systems. The elegant way of describing the search interval for each unknown is to consider material parameters as a positive real numbers (0, Inf), the effective angle  $\Theta_0$  in

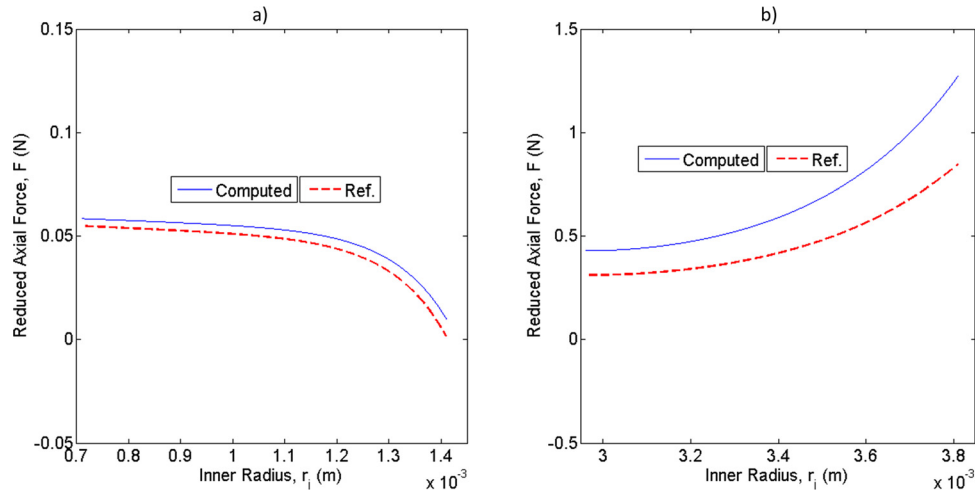


**Fig. 4 Axial force distribution through the arterial wall in (a) rabbit carotid artery and (b) human carotid artery compared with results (Ref.) based on in vitro experiments [22]**

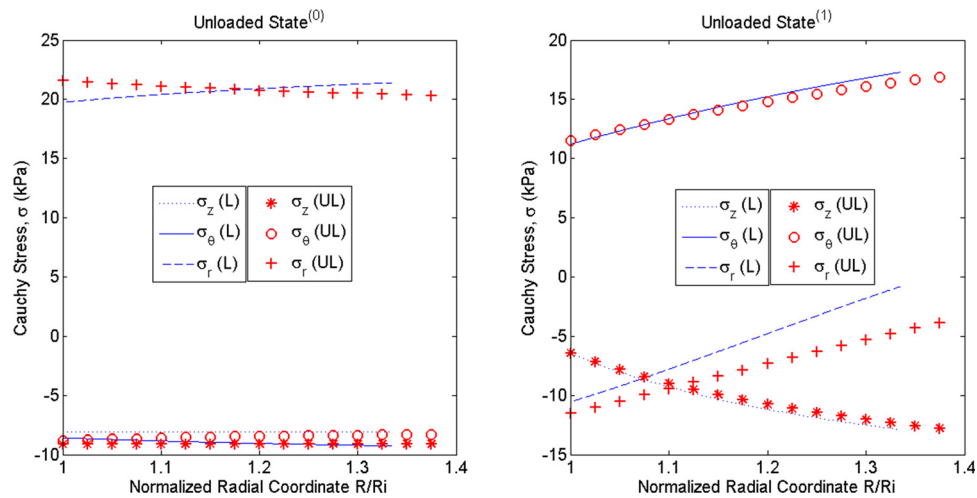


**Fig. 5 Residual stress distribution through the arterial wall in unloaded state<sup>(0)</sup> and unloaded state<sup>(1)</sup> in swine iliac artery during the loading (L) and unloading (UL)**

**Table 7 Numerical values of constants appearing in 11 PM, where material parameters and residual strain parameters are computed using experimental data points from the physiological state of swine iliac artery in loading and unloading states, respectively.**

States	$c$ (kPa)	Material parameters						Residual strain parameters			
		$b_1$	$b_2$	$b_3$	$b_4$	$b_5$	$b_6$	$\Theta_0$ (deg)	$R_i$ (mm)	$R_o$ (mm)	$\lambda_z$
Loading	16.08	0.0198	0.0645	7.2365	4.9803	0.8747	1.9429	110.1	2.60	3.47	1.22
Unloading	16.93	0.0000	0.0000	7.3053	4.9788	0.7731	1.8210	121.9	2.61	3.64	1.22

the interval (0 deg, 180 deg), the axial prestretch  $\lambda_z$  in the interval (1.0, 2.0), and the effective radii  $R_i$  and  $R_o$  in the interval ( $r_i^{(LDP)}$ ,  $2 r_i^{(LDP)}$ ) and ( $r_o^{(LDP)}$ ,  $2 r_o^{(LDP)}$ ), where  $r_i^{(LDP)}$  and  $r_o^{(LDP)}$  are the inner radius and outer radius in the lowest value of diastolic pressure, respectively. Another important point is the selection of initial estimates for each unknown, where each initial estimate is selected arbitrarily in defined intervals. After the first iteration, the computed parameters are used as the initial estimates for the second iteration in order to improve the accuracy of computed parameters.

One of the main goals of the present study was to validate proposed mathematical technique by performing subsequent computations in various realistic scenarios. It can be pointed out that computed results are strongly independent from the number of experimental data points and addition of Gaussian noise to the same data sets exhibiting well qualitative agreement with their in vitro counterparts (Tables 2–5). Figures 3–5 demonstrate adequate fit of the computed residual stresses with residual stresses plotted based on parameters obtained from in vitro measurements.



**Table 8 Numerical values of constants appearing in 11 PM, where material parameters and residual strain parameters are predicted both for *baseline* and *remodeled* rabbit carotid artery using data points (pressure and diameter) obtained from the finite element model (FEM). Baseline (FEM) values are the same values presented in Ref. [22], where remodeled (FEM) values have the same material parameters as baseline (FEM) but with altered residual strain parameters (e.g., the effective angle decreased to 90 deg. from 100 deg.) simulated in ADINA.**

Material property	$c$ (kPa)	Material parameters						Residual strain			
		$b_1$	$b_2$	$b_3$	$b_4$	$b_5$	$b_6$	$\Theta_0$ (deg)	$R_i$ (mm)	$R_o$ (mm)	$\lambda_z$
Baseline	22.59	0.0529	0.0039	0.0284	0.0082	0.0000	0.0181	101.8	1.73	1.86	1.60
Remodeled	28.18	4.3329	0.3217	0.4987	0.9352	0.0358	0.6474	89.8.1	1.89	1.94	1.66
Baseline (FEM)	<b>26.95</b>	<b>0.9925</b>	<b>0.4180</b>	<b>0.0089</b>	<b>0.0749</b>	<b>0.0295</b>	<b>0.0193</b>	<b>100.0</b>	<b>1.43</b>	<b>1.82</b>	<b>1.70</b>
Remodeled (FEM)	—	—	—	—	—	—	—	<b>90.0</b>	<b>1.61</b>	<b>2.00</b>	<b>1.70</b>

In the case of in vivo estimation of residual strains and stresses, associated parameters and stress distribution slightly differ for the loading and unloading states, while computed in vivo axial prestretch values were the same (Table 7). These variations present a novel message about the viscoelastic mechanical response of soft tissues demonstrating the pressure dependent remodeling in two subsequent loading and unloading states occurring during one cardiac cycle.

For highly curved vessels and three-dimensional patient specific arteries and veins, a similar analytical formulation can be derived that includes the vessel curvature. While it may also feasible to partition the cylindrical vascular tube into several circular rings each having a finite thickness. This partitioned model can be analyzed based on a finite element formulation, and residual strain parameters and material parameters can be computed for each of the ring domain using the corresponding segmental experimental pressure–radius (diameter) data points obtained through in vivo measurement techniques.

In conclusion, it is merely sufficient to have knowledge of in vivo pressure–radius (diameter) relation in order to estimate residual strains and stresses in the vascular system. Therewithal, it should be emphasized that kinematic formulations presented in this study are based on assumptions of incompressible, homogeneous, and cylindrically orthotropic vessel wall, and constitutive relations do not take into account the mechanical response of each microstructure elements such as collagen, elastin, and smooth muscle fibers considering the hyperelastic behavior of whole vascular tissue. However, the proposed mathematical technique does not restrict the choice of strain energy formulation (as in our finite element model that includes vessel constituents); contrariwise microstructure models will introduce physical meanings of material parameters such as density and orientation of fibers and other complexities.

While the pulsatile pressure data can be obtained routinely through cardiac catheterization procedure for the specific vessel, the noninvasive pressure measurement techniques are also advancing and becoming available in clinics as an alternative. For example, the patient specific pressure pulse wave can be acquired continuously [32,33] including the pulse-oximetry devices correlating with the pressure waveform or through magnetic resonance imaging [34]. Although these techniques are still in development phase, there are several encouraging results acquired with them [35–38]. Our proposed methodology can be integrated with these measurement modalities. Noninvasive techniques generally need a calibration step to estimate the pressure at the specific arterial vessel. One calibration approach is based on the auscultatory method, which measures absolute systolic blood pressure and diastolic blood pressure noninvasively. The vessel radii can also be calculated noninvasively through ultrasound monitoring. Both flow and pressure data can be gated with electrocardiography and thus synchronized. We applied this approach to study synchronized flow/pressure waveforms in congenital heart patients [39]. In summary, clinical data required for our methodology are available with today's techniques [31]. In the future, we will implement this

validated technique to the experimental data set acquired in our laboratory using simultaneous optical coherence tomography [40] and servo-null pressure measurements of chick embryonic vessels, particularly embryonic great arteries [41]. This will provide the time-resolved growth rate of embryonic vessels and relate with the stress-dependent finite growth models. Another important application is the in vitro testing of small-sized vessels, which can be used to validate the present theoretical results further.

## 5 Conclusion

All known techniques for estimating residual stresses are *invasive* and to our knowledge present technique is the first *noninvasive* methodology that can compute residual stress parameter in vivo, using standard clinical measurements. One of the additional message is that the residual stress distribution changes dramatically, while in vivo axial prestretch is present. The most striking point is that instead of performing in vitro experiments to measure residual strain parameters, it is merely sufficient to use the cuff pressure, pressure–inner radius data obtained from diastolic–systolic pressure waveform by noninvasive clinical or biological measurement techniques, in order to determine residual strains and stresses. Present technique can allow the prediction of local vessel growth due to an intended surgical intervention. Once residual strains and stresses are computed, stress-dependent finite growth models can be used to analyze the growth of vascular tissue belonging to specific patient. A segmental circumferential averaged formulation version can also allow the in vivo mapping of material properties as well as residual stresses along the vessel axis where properties are variable [42].

## Acknowledgment

This work was supported by the European Research Council (ERC) Starting Grant—Vascular Growth project #307460 and the Scientific and Technical Research Council of Turkey (TUBITAK), 2215—Graduate Scholarship Program for International Students.

## References

- [1] Fung, Y. C., 1991, "What Are the Residual Stresses Doing in Our Blood Vessels?," *Ann. Biomed. Eng.*, **19**(3), pp. 237–249.
- [2] Frobert, O., Gregersen, H., Bjerre, J., Bagger, J. P., and Kassab, G. S., 1998, "Relation Between Zero-Stress State and Branching Order of Porcine Left Coronary Arterial Tree," *Am. J. Physiol.*, **275**(6 Pt. 2), pp. H2283–H2290.
- [3] Merodio, J., Ogden, R. W., and Rodríguez, J., 2013, "The Influence of Residual Stress on Finite Deformation Elastic Response," *Int. J. Non-Linear Mech.*, **56**, pp. 43–49.
- [4] Rachev, A., and Greenwald, S. E., 2003, "Residual Strains in Conduit Arteries," *J. Biomech.*, **36**(5), pp. 661–670.
- [5] Costa, M. F. M., and Teixeira, V., 2011, "Residual Stress Measurement in PVD Optical Coatings by Microtopography," *Measurement*, **44**(3), pp. 549–553.
- [6] Scruby, C. B., Antonelli, G., Buttle, D. J., Dalzell, W., Gori, M., Gulliver, J. A., de Michelis, C., Ravenscroft, F. A., and Ruzzier, M., 1996, "Development of Non-Invasive Methods for Measurement of Stress in Welded Steel Structures," *Eur. J. Non-Destr. Test.*, **3**(2), pp. 46–54.

- [7] Fung, Y. C., Fronek, K., and Patitucci, P., 1979, "Pseudoelasticity of Arteries and the Choice of Its Mathematical Expression," *Am. J. Physiol.*, **237**(5), pp. H620-H631.
- [8] Chuong, C. J., and Fung, Y. C., 1986, "On Residual Stresses in Arteries," *ASME J. Biomech. Eng.*, **108**(2), pp. 189-192.
- [9] Takamizawa, K., and Hayashi, K., 1987, "Strain Energy Density Function and Uniform Strain Hypothesis for Arterial Mechanics," *J. Biomech.*, **20**(1), pp. 7-17.
- [10] Omens, J. H., and Fung, Y. C., 1990, "Residual Strain in Rat Left Ventricle," *Circ. Res.*, **66**(1), pp. 37-45.
- [11] Summerour, S. R., Emery, J. L., Fazeli, B., Omens, J. H., and McCulloch, A. D., 1998, "Residual Strain in Ischemic Ventricular Myocardium," *ASME J. Biomech. Eng.*, **120**(6), pp. 710-714.
- [12] Weis, S. M., Emery, J. L., Becker, K. D., McBride, D. J., Jr., Omens, J. H., and McCulloch, A. D., 2000, "Myocardial Mechanics and Collagen Structure in the Osteogenesis Imperfecta Murine (Oim)," *Circ. Res.*, **87**, pp. 663-669.
- [13] Liu, S. Q., and Fung, Y. C., 1992, "Influence of STZ-Induced Diabetes on Zero-Stress States of Rat Pulmonary and Systemic Arteries," *Diabetes*, **41**(2), pp. 136-146.
- [14] Pang, Q., Lu, X., Gregersen, H., von Oettingen, G., and Astrup, J., 2001, "Biomechanical Properties of Porcine Cerebral Bridging Veins With Reference to the Zero-Stress State," *J. Vasc. Res.*, **38**(1), pp. 83-90.
- [15] Han, H. C., and Fung, Y. C., 1991, "Residual Strains in Porcine and Canine Trachea," *J. Biomech.*, **24**(5), pp. 307-315.
- [16] Xu, G., Kemp, P. S., Hwu, J. A., Beagley, A. M., Bayly, P. V., and Taber, L. A., 2010, "Opening Angles and Material Properties of the Early Embryonic Chick Brain," *ASME J. Biomech. Eng.*, **132**(1), p. 011005.
- [17] Taber, L. A., Hu, N., Pexieder, T., Clark, E. B., and Keller, B. B., 1993, "Residual Strain in the Ventricle of the Stage 16-24 Chick Embryo," *Circ. Res.*, **72**(2), pp. 455-462.
- [18] Alford, P. W., and Taber, L. A., 2008, "Computational Study of Growth and Remodelling in the Aortic Arch," *Comput. Methods Biomech. Biomed. Eng.*, **11**(5), pp. 525-538.
- [19] Wang, R., and Gleason, R. L., Jr., 2010, "A Mechanical Analysis of Conduit Arteries Accounting for Longitudinal Residual Strains," *Ann. Biomed. Eng.*, **38**(4), pp. 1377-1387.
- [20] Lu, X., Zhao, J. B., Wang, G. R., Gregersen, H., and Kassab, G. S., 2001, "Remodeling of the Zero-Stress State of Femoral Arteries in Response to Flow Overload," *Am. J. Physiol. Heart Circ. Physiol.*, **280**(4), pp. H1547-H1559.
- [21] Bischoff, J. E., Arruda, E. A., and Grosh, K., 2002, "A Microstructurally Based Orthotropic Hyperelastic Constitutive Law," *ASME J. Appl. Mech.*, **69**(5), pp. 570-579.
- [22] Holzapfel, G., Gasser, T., and Ogden, R., 2000, "A New Constitutive Framework for Arterial Wall Mechanics and a Comparative Study of Material Models," *J. Elasticity Phys. Sci. Solids*, **61**(1-3), pp. 1-48.
- [23] Zhang, Y., Dunn, M. L., Drexler, E. S., McCowan, C. N., Slifka, A. J., Ivy, D. D., and Shandas, R., 2005, "A Microstructural Hyperelastic Model of Pulmonary Arteries Under Normo- and Hypertensive Conditions," *Ann. Biomed. Eng.*, **33**(8), pp. 1042-1052.
- [24] Chuong, C. J., and Fung, Y. C., 1983, "Three-Dimensional Stress Distribution in Arteries," *ASME J. Biomech. Eng.*, **105**(3), pp. 268-274.
- [25] Delfino, A., Stergiopoulos, N., Moore, J. E., Jr., and Meister, J. J., 1997, "Residual Strain Effects on the Stress Field in a Thick Wall Finite Element Model of the Human Carotid Bifurcation," *J. Biomech.*, **30**(8), pp. 777-786.
- [26] Mekkaoui, C., Friggi, A., Rolland, P. H., Bodard, H., Piquet, P., Bartoli, J. M., and Mesana, T., 2001, "Simultaneous Measurements of Arterial Diameter and Blood Pressure to Determine the Arterial Compliance, Wall Mechanics and Stresses In Vivo," *Eur. J. Vasc. Endovascular Surg.*, **21**(3), pp. 208-213.
- [27] Belousov, L. V., Saveliev, S. V., Naumidi, I. I., and Novoselov, V. V., 1994, "Mechanical Stresses in Embryonic Tissues: Patterns, Morphogenetic Role, and Involvement in Regulatory Feedback," *Int. Rev. Cytol.*, **150**, pp. 1-34.
- [28] Rodriguez, E. K., Hoger, A., and McCulloch, A. D., 1994, "Stress-Dependent Finite Growth in Soft Elastic Tissues," *J. Biomech.*, **27**(4), pp. 455-467.
- [29] Kowalski, W. J., Teslovich, N. C., Menon, P. G., Tinney, J. P., Keller, B. B., and Pekkan, K., 2014, "Left Atrial Ligation Alters Intracardiac Flow Patterns and the Biomechanical Landscape in the Chick Embryo," *Dev. Dyn.*, **243**(5), pp. 652-662.
- [30] Restrepo, M., Mirabella, L., Tang, E., Haggerty, C. M., Khiabani, R. H., Fynn-Thompson, F., Valente, A. M., McElhinney, D. B., Fogel, M. A., and Yoganathan, A. P., 2014, "Fontan Pathway Growth: A Quantitative Evaluation of Lateral Tunnel and Extracardiac Cavopulmonary Connections Using Serial Cardiac Magnetic Resonance," *Ann. Thorac. Surg.*, **97**(3), pp. 916-922.
- [31] Taber, L. A., 2009, "Towards a Unified Theory for Morphomechanics," *Philos. Trans. R. Soc. A*, **367**(1902), pp. 3555-3583.
- [32] Saugel, B., Dueck, R., and Wagner, J. Y., 2014, "Measurement of Blood Pressure," *Best Pract. Res. Clin. Anaesthesiol.*, **28**(4), pp. 309-322.
- [33] Naik, B. I., and Durieux, M. E., 2014, "Hemodynamic Monitoring Devices: Putting it All Together," *Best Pract. Res. Clin. Anaesthesiol.*, **28**(4), pp. 477-488.
- [34] Quail, M. A., Steeden, J. A., Knight, D., Segers, P., Taylor, A. M., and Muthurangu, V., 2014, "Development and Validation of a Novel Method to Derive Central Aortic Systolic Pressure From the MR Aortic Distension Curve," *J. Magn. Reson. Imaging*, **40**(5), pp. 1064-1070.
- [35] Meidert, A. S., Huber, W., Muller, J. N., Schofthaler, M., Hapfelmeier, A., Langwieser, N., Wagner, J. Y., Eyer, F., Schmid, R. M., and Saugel, B., 2014, "Radial Artery Applanation Tonometry for Continuous Non-Invasive Arterial Pressure Monitoring in Intensive Care Unit Patients: Comparison With Invasively Assessed Radial Arterial Pressure," *Br. J. Anaesth.*, **112**(3), pp. 521-528.
- [36] Janelle, G. M., and Gravenstein, N., 2006, "An Accuracy Evaluation of the T-Line Tensymeter (Continuous Noninvasive Blood Pressure Management Device) Versus Conventional Invasive Radial Artery Monitoring in Surgical Patients," *Anesth. Analg.*, **102**(2), pp. 484-490.
- [37] Szmuk, P., Pivalizza, E., Warters, R. D., Ezri, T., and Gebhard, R., 2008, "An Evaluation of the T-Line<sup>®</sup> Tensymeter Continuous Noninvasive Blood Pressure Device During Induced Hypotension," *Anaesthesia*, **63**(3), pp. 307-312.
- [38] Meidert, A. S., Huber, W., Hapfelmeier, A., Schofthaler, M., Muller, J. N., Langwieser, N., Wagner, J. Y., Schmid, R. M., and Saugel, B., 2013, "Evaluation of the Radial Artery Applanation Tonometry Technology for Continuous Noninvasive Blood Pressure Monitoring Compared With Central Aortic Blood Pressure Measurements in Patients With Multiple Organ Dysfunction Syndrome," *J. Crit. Care*, **28**(6), pp. 908-912.
- [39] Hong, H., Dur, O., Zhang, H., Zhu, Z., Pekkan, K., and Liu, J., 2013, "Fontan Conversion Templates: Patient-Specific Hemodynamic Performance of the Lateral Tunnel Versus the Intraatrial Conduit With Fenestration," *Pediatr. Cardiol.*, **34**(6), pp. 1447-1454.
- [40] Kowalski, W. J., Teslovich, N. C., Chen, C.-Y., Keller, B. B., and Pekkan, K., 2014, "Simultaneous Real-Time Quantification of Blood Flow and Vascular Growth in the Chick Embryo Using Optical Coherence Tomography," *Proc. SPIE* **8953**, p. 895307.
- [41] Lindsey, S. E., Menon, P. G., Kowalski, W. J., Shekhar, A., Yalcin, H. C., Nishimura, N., Schaffer, C. B., Butcher, J. T., and Pekkan, K., 2014, "Growth and Hemodynamics After Early Embryonic Aortic Arch Occlusion," *Biomech. Model. Mechanobiol.*
- [42] Maher, E., Early, M., Creane, A., Lally, C., and Kelly, D. J., 2012, "Site Specific Inelasticity of Arterial Tissue," *J. Biomech.*, **45**(8), pp. 1393-1399.